Supporting Information:

Activating Interfacial Polarization via Snowflake–Sphere Dual-Vacancy Heterostructures for Efficient S-scheme Photocatalytic Hydrogen Evolution

Hongyu Zhao [a], Zheng Wang [a], Fenghuan Zhao [b], Xu, Sun [a], Yuhang Wang [a], Chunchao Hou [a], Junjie Qin [a], Haiyan Li [a], Bohua Dong [a,], Lixin Cao [a,]* and Chenghui Xia [a,]**

a. School of Materials Science and Engineering, Ocean University of China, No. 1299, Sansha Road, Huangdao District, Qingdao, 266404, PR China

b. Department of Mechanical and Electrical Engineering, Rizhao Polytechnic, 16 Yantai North Road, Rizhao City, Shandong Province, 276826, PR China

*Corresponding author:

E-mail: dongbohua@ouc.edu.cn; caolixin@ouc.edu.cn; c.xia@ouc.edu.cn

Characterization

High-resolution transmission electron microscopy (HRTEM), TEM, and EDS analyses were conducted using a Thermo Scientific Talos F200X G2 TEM equipped with a Super-X EDS system (four silicon drift detectors). Samples were deposited on 300-mesh nickel grids, with imaging and spectroscopy performed at 200 kV acceleration voltage, respectively. Morphologicaland microstructural features of the samples were investigated using scanning electronmicroscopy (SEM, Gemini 300, Zeiss and SU 8220/8100, HITACHI). X-Ray diffraction (XRD) measurements were conducted using a Bruker D8 Advance X-Ray diffractometer with Cu Kα radiation (λ = 1.5406 Å). The absorption spectra of all materials were measured using a UV-2500 (Shimadzu, Japan) spectrophotometer. Fluorescence spectra (PL) were measured using a FLS 980 series of fluorescence spectrometers (EI, UK). X-Ray photoelectron spectroscopy (XPS) measurement was performed on a Thermo Scientific ESCALAB 250 Xi instrument equipped with a twin-crystal microfocusing X-ray monochromator and a double-focusing full 180° spherical sector analyzer. The binding energy (BE) of each element was calibrated by setting the C1s line of adventitious hydrocarbon to a BE of 284.80 eV. The BET surface area and pore diameter distribution of the photocatalysts were carried out using a Tristar 3020 system (Micromeritics Instrument Corp). Electron paramagnetic resonance (EPR) measurements were performed on a EPR 200 instrument (KYKY CO., LTD) with 0 (darkness), and 1 min of light. All dark-state measurements were performed in a fully enclosed light-tight chamber. Before measurement, the reaction suspensions were deoxygenated with high-purity Ar for 30 min, and the dissolved oxygen level was below 0.05 mg L^{-1}. Control tests include catalyst-only, DMPO-only, and catalyst without sacrificial agents. No radical signals were observed in any control tests. Each experiment was repeated three times to reduce the fluctuation. Zeta Potential measurements were performed on a NanoBrook 90PLUS PALS instrument (Brookhaven, US). All the static contact angle of water droplets were measured with optical contact angle meter (JC2000DM) at room temperature. A droplet volume of 4 μL. The average contact angle of five different points was used to characterize the wettability of the sample.

Photoelectrochemical measurements

The PEC measurements were conducted using an electrochemical workstation (CHI660E, ChenHua Instruments, Inc., Shanghai) under irradiation from a 300 W Xenon lamp (Beijing, CEAULIGHT), with the average radiation intensity maintained at 100 mW cm^{-2}. A standard three-electrode setup was employed for the tests. The working electrode was prepared by spin-coating the photocatalysts onto a 1×1 cm^2 FTO glass electrode, followed by vacuum drying at 60 ℃ overnight. A 0.5 mol/L Na_2SO_4 solution served as the electrolyte. Transient photocurrent-time curves were recorded under a bias voltage of -0.4 V *vs*. Ag/AgCl, with the light turned on and off. Electrochemical impedance spectroscopy was performed using an impedance analyzer over a frequency range from 10^5 to 10^{-1} Hz. Mott–Schottky plots were obtained at 1000 Hz with potential scanned from –1.0 to +1.0 V (vs. Ag/AgCl) in the dark, and the flat-band potentials were converted to the normal hydrogen electrode (NHE) scale for band alignment analysis. The cyclic voltammetry (CV) curves were recorded within the potential at scan rates ranging from 0.01 to 0.1 V s^{-1}. The electrochemical active surface area (ECSA) was estimated from the double-layer capacitance (Cdl) derived from the slope of the CV current density versus scan rate. All measurements for different samples were carried out under identical conditions to ensure reliable comparison.

Photocatalytic hydrogen evolution performance test

To measure the photocatalytic activity of HER, a self-made offline flow sampling system was adopted. The quartz reactor was connected to the gas chromatograph (GC-7920, Beijing China Education Au-light Co.Ltd) with nitrogen as the carrier gas, and hydrogen was detected using a thermal conductivity detector (TCD). In a 100 mL reactor, 5.0 mg of the photocatalyst was dispersed in an aqueous solution containing a pore remover (0.25 M Na_2S, 0.35 M Na_2SO_3, 10 ml aqueous solution). Before measurement, the system is degassed to remove the air in the reactor and then filled with nitrogen. Then, a 300 W xenon lamp (CEL-HXF300, Beijing China Education Au-light Co.Ltd) was used, with the average radiation intensity maintained at 100 mW cm^{-2}, and the samples were irradiated with a 420 nm longpass filter. The lamp is placed 6 centimeters away from the reactor. The reaction temperature is maintained at 5 ℃ by using a cooling plate. In addition, we conducted a blank experiment without samples, proving that the thermal effect can be ignored. To determine the hydrogen production, we extracted 0.5 mL of gas from a 100 ml reactor and injected it into the gas chromatograph. Then, we read the peak area of the hydrogen and converted it into the hydrogen production through a standard curve.

DFT Calculations

The density functional theory (DFT) calculations were carried out with the VASP code[1]. The Perdew-Burke-Ernzerhof (PBE) functional within generalized gradient approximation (GGA)[2] was used to process the exchange-correlation, while the projectoraugmented-wave pseudopotential (PAW)[3] was applied with a kinetic energy cut-off of 500 eV, which was utilized to describe the expansion of the electronic eigenfunctions. The vacuum thickness was set to be 15 Å to minimize interlayer interactions. The Brillouin-zone integration was sampled by a Γ-centered 7 × 7 × 1 Monkhorst–Pack k-point. All atomic positions were fully relaxed until energy and force reached a tolerance of 1×10^{-6} eV and 0.01 eV/Å, respectively. The dispersion corrected DFT-D method was employed to consider the long-range interactions[4]. The $Cu_{2-x}S/ZnCdS_v$ interface was constructed from optimized (001)/(100) slabs, and the interfacial dipole moment was derived from the differential charge density (Δρ) according to $\mu = \int r\Delta\rho(r)d\,r$. Bader charge analysis was further used to quantify the interfacial charge transfer.

Supplementary Figures

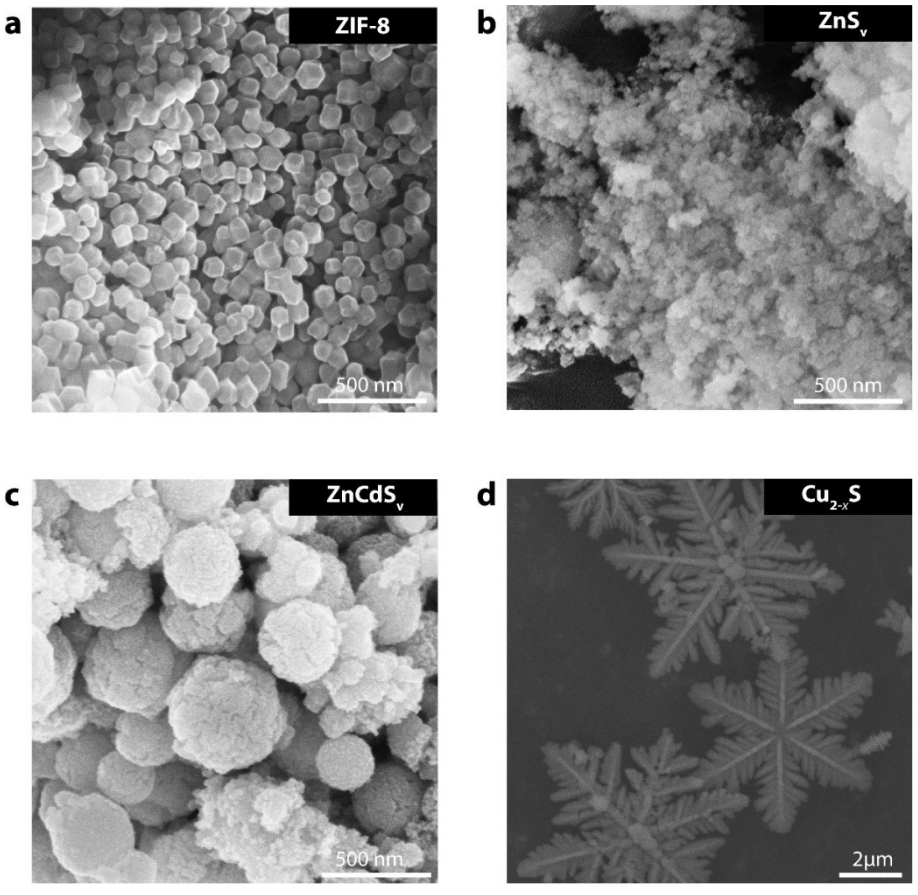

Fig. S1. Scanning electron microscopy (SEM) images: **(a)** Pristine ZIF-8 particles (average size ~80 nm). **(b)** ZnS_v derived from sulfurization of ZIF-8. **(c)** $ZnCdS_v$ formed via cation exchange. **(d)** Snowflake-like $Cu_{2-x}S$ nanostructures.

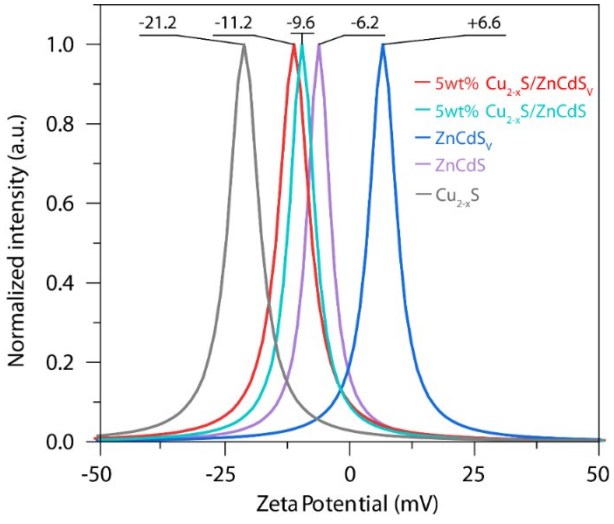

Fig. S2. Zeta potential of $Cu_{2-x}S$, ZnCdS, $ZnCdS_v$, 5wt% $Cu_{2-x}S$/ZnCdS and 5wt% $Cu_{2-x}S$/$ZnCdS_v$ in aqueous solution (pH 7.0).

.

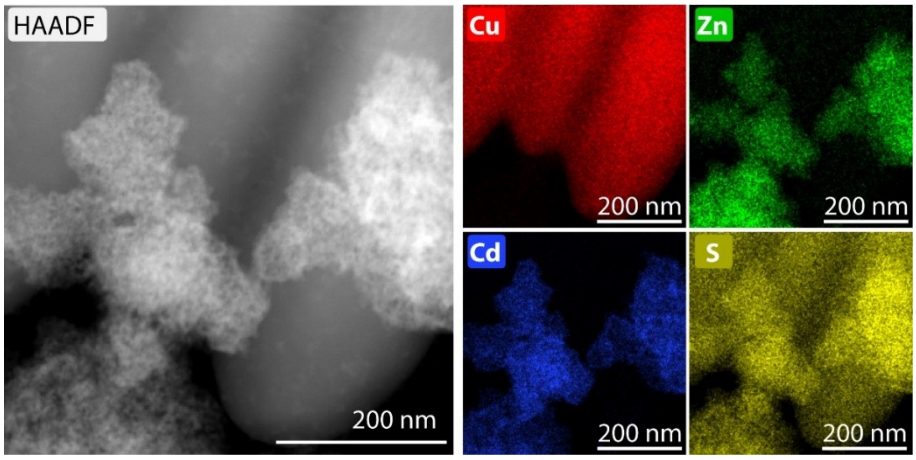

Fig. S3. Elemental maps of 5wt% $Cu_{2-x}S/ZnCdS_v$ heterostructure.

.

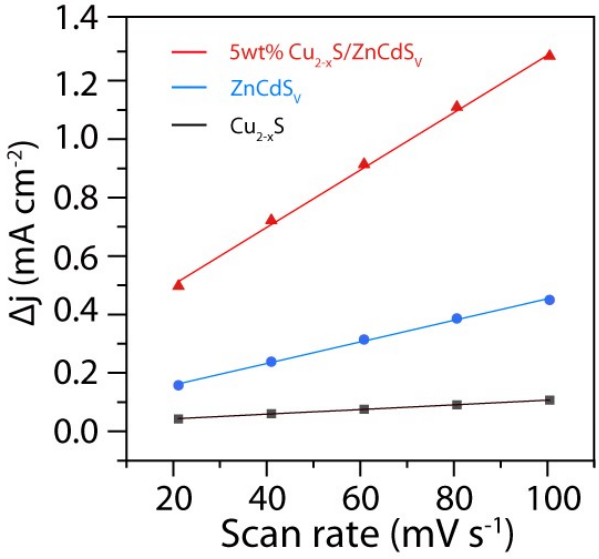

Fig. S4. ECSA evaluation of $Cu_{2-x}S$, $ZnCdS_v$ and 5wt% $Cu_{2-x}S/ZnCdS_v$.

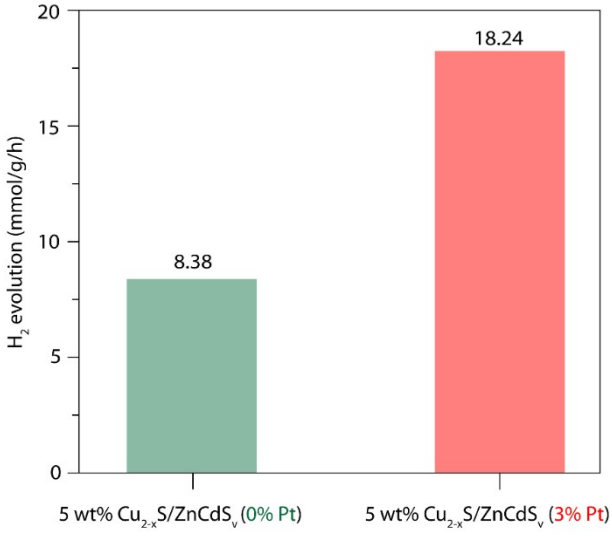

Fig. S5. Photocatalytic hydrogen evolution performance comparison of 5wt% $Cu_{2-x}S/ZnCdS_v$ composite under co-catalyst-free conditions versus with 3wt% Pt co-catalyst.

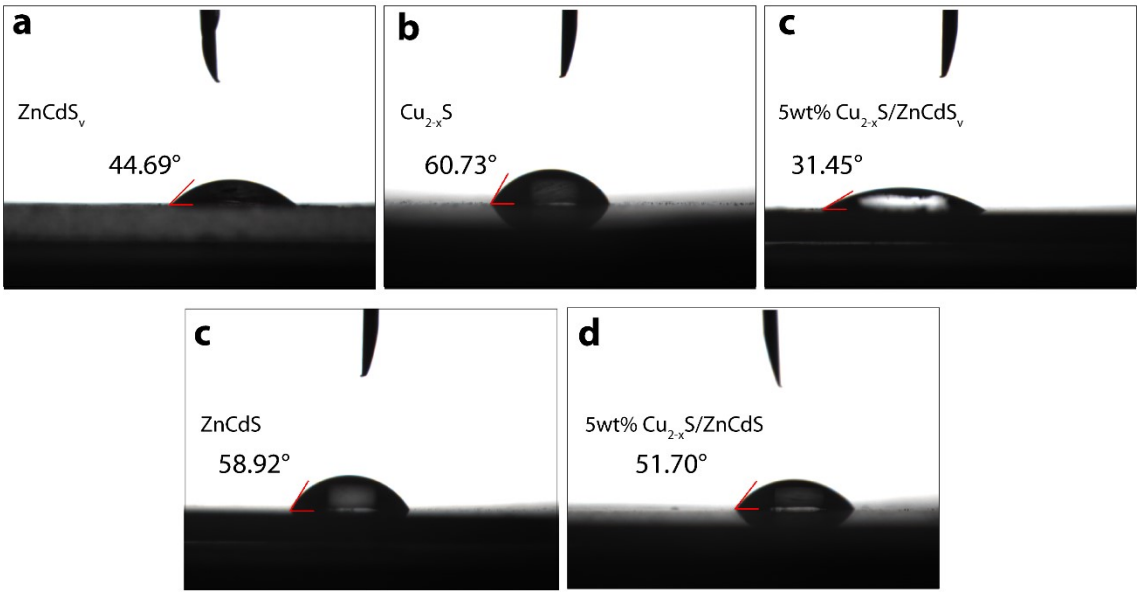

Fig. S6. Water contact angle measurements: **(a)**ZnCdS$_v$: 44.69°, **(b)** Cu$_{2-x}$S: 60.73°, **(c)** 5wt% Cu$_{2-x}$S/ZnCdS$_v$: 31.45°, **(d)** ZnCdS: 58.92°, **(e)** 5wt% Cu$_{2-x}$S/ZnCdS: 51.70°.

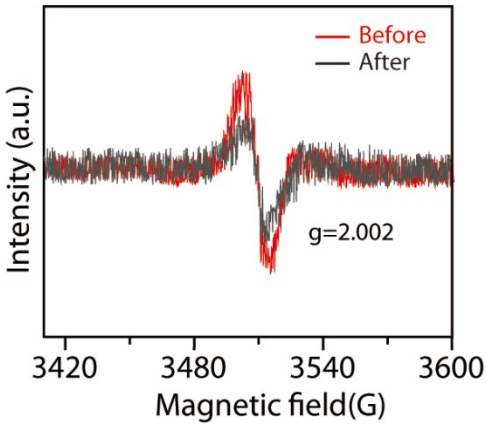

Fig. S7. EPR spectra of 5wt% Cu$_{2-x}$S/ZnCdS$_v$ before and after four photocatalytic cycles.

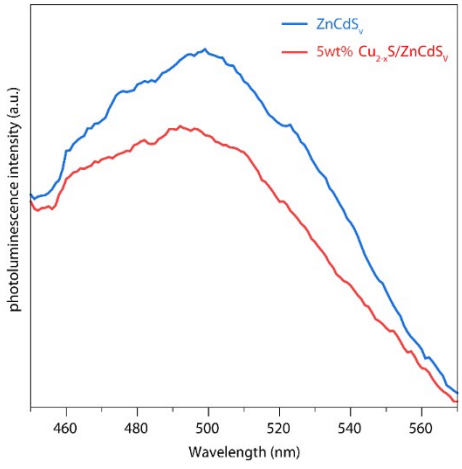

Fig. S8. Photoluminescence spectra of $ZnCdS_v$ nanocrystals and 5wt% $Cu_{2-x}S/ZnCdS_v$ composites.

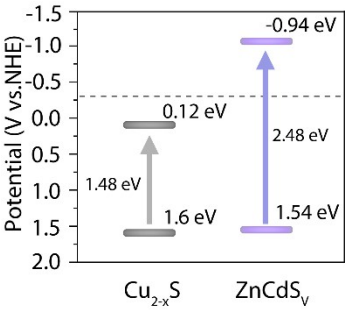

Fig. S9. Band alignment diagram for $Cu_{2-x}S$ and $ZnCdS_v$ derived from the Mott-Schottky analysis and the optical bandgaps.

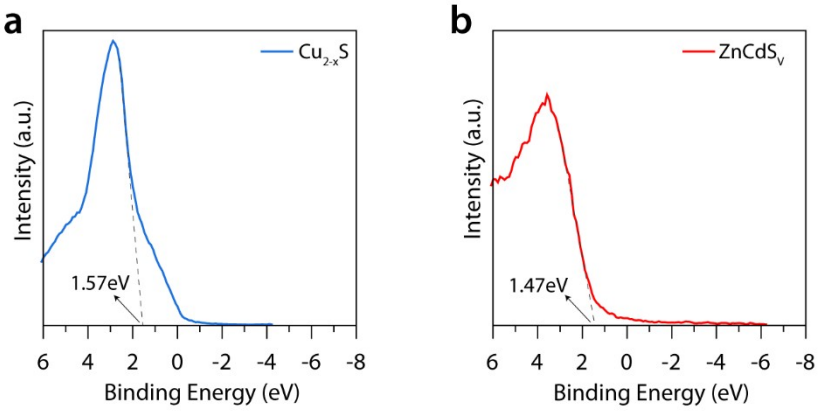

Fig. S10. Valence band XPS spectra referenced to the standard hydrogen electrode potential: **(a)** $Cu_{2-x}S$ valence band maximum located at 1.57 V. **(b)** $ZnCdS_v$ valence band maximum positioned at 1.47 eV.

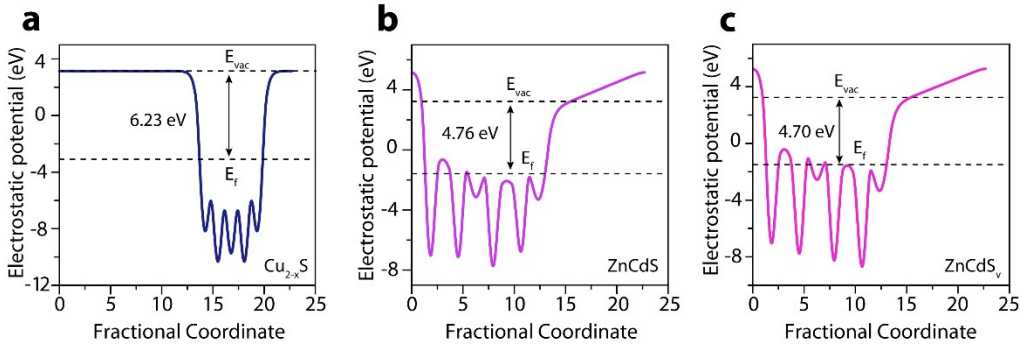

Fig. S11. Work functions of **(a)** $Cu_{2-x}S$, **(b)** ZnCdS and **(c)** $ZnCdS_v$ derived from DFT calculations.

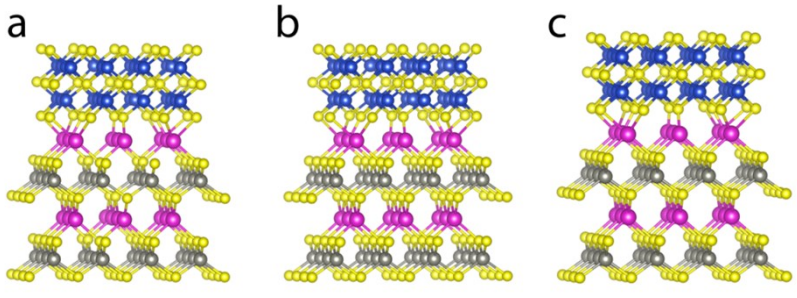

Fig. S12. DFT-simulated atomic models of heterointerfaces: **(a)** $Cu_{2-x}S/ZnCdS_v$ (dual vacancies), **(b)** $Cu_{2-x}S/ZnCdS$ (Cu vacancies only), **(c)** $Cu_2S/ZnCdS$ (stoichiometric).

Supplementary Tables

Table S1. Elemental composition of Cu, Zn, Cd, and S shown in **Fig. S3.**

Element	Family	Atomic Fraction (%)	Atomic Error (%)	Mass Fraction (%)	Mass Error (%)	Fit Error (%)
Cu	K	45.28	3.61	52.91	3.74	0.03
Zn	K	8.21	1.14	9.88	1.41	0.02
Cd	L	6.62	1.14	13.69	1.73	0.08
S	K	39.89	2.66	23.52	1.86	0.11

Table S2. The atomic fractions of Cu, S, Cd, Zn by XPS.

Sample	Cu 2p(%)	Zn 2p(%)	Cd 3d(%)	S 2p(%)
$Cu_{2-x}S$	63.1			36.9
ZnCdS		32.4	26.3	41.3
$Cu_{2-x}S$/ZnCdS	7.53	29.87	22.7	39.3

Table S3. Specific surface area of $Cu_{2-x}S$，$ZnCdS_v$ and 5wt% $Cu_{2-x}S/ZnCdS_v$ heterojunction.

Samples	**S_{BET} (m^2/g)**
$Cu_{2-x}S$	31.71
$ZnCdS_v$	90.26
5wt% $Cu_{2-x}S/ZnCdS_v$	102.2

Table S4. ZnCdS-based photocatalysts illuminated under visible light (λ > 420nm).

Photocatalyst	**co-catalyst**	**Mass**	**HER (μmol h^{-1} g^{-1})**	**Ref.**
5 wt% $Cu_{2-x}S/ZnCdS_v$	None	5 mg	8380	This work
	Pt	5 mg	18200	This work
Vs-ZnCdS/NiMnS	None	10 mg	1964.8	Ref[5]
ZnCdS/HEA	HEA	10 mg	5990	Ref[6]
ZnCdS(EDA)/Ni@NiO	None	5 mg	5760	Ref[7]
$Zn_{0.5}Cd_{0.5}S/Co_3O_4$	None	5 mg	6720	Ref[8]
ZnS/ZnCdS	None	10 mg	2920	Ref[9]

References

1. G. Kresse and J. Furthmuller, Efficiency of ab-initio total energy calculations for metals and semiconductors using a plane-wave basis set. *Comput. Mater. Sci.*, 1996, **6**, 15-50.
2. J. P. Perdew, K. Burke and M. Ernzerhof, Generalized gradient approximation made simple (vol 77, pg 3865, 1996). *Phys. Rev. Lett.*, 1997, **78**, 1396-1396.
3. P. E. Blochl, Projector augmented-wave method. *Phys. Rev. B*, 1994, **50**, 17953-17979.
4. S. Grimme, Semiempirical GGA-type density functional constructed with a long-range dispersion correction. *J. Comput. Chem.*, 2006, **27**, 1787-1799.
5. L. Ding, X. Y. Zhang, M. J. Lei, X. L. Ma, Y. J. Li and Z. L. Jin, Surface engineering modulation and optimization of S-vacancy ZnCdS combined with NiMnS for efficient photocatalytic hydrogen evolution. *Appl. Catal. A-Gen.*, 2025, **704**, 120415.
6. J. Wang, X. Y. Niu, R. Wang, K. Zhang, X. Y. Shi, H. Y. Yang, J. L. Ye and Y. P. Wu, High-entropy alloy-enhanced ZnCdS nanostructure photocatalysts for hydrogen production. *Appl. Catal. B-Environ. Energy*, 2025, **362**, 124763.
7. C. Y. Guo, Y. Y. Zou, Y. Q. Ma, N. Akram, A. Ahmad and J. D. Wang, Construction of one-dimensional ZnCdS(EDA)/Ni@NiO for photocatalytic hydrogen evolution. *Dalton Trans.*, 2024, **53**, 3731-3743.
8. T. X. Zhang, F. L. Meng, M. M. Gao, J. S. Wei, K. J. H. Lim, K. H. Lim, P. Chirawatkul, A. S. W. Wong, S. Kawi and G. W. Ho, Porous host-guest MOF-semiconductor hybrid with multisites heterojunctions and modulable electronic band for selective photocatalytic CO_2 conversion and H_2 evolution. *Small*, 2023, **19**, 2301121.
9. J. P. Song, J. L. Li, Y. Zhuang, D. X. Guo, S. Meng, D. T. Zhang, X. Yang, Y. Li and G. Z. Sui, Grain boundary engineering-assisted Cu in-situ doped ZnS/ZnCdS heterojunction for boosting photocatalytic hydrogen evolution. *Sep. Purif. Technol.*, 2025, **367**, 132889.